Improving the Accuracy and Spatial Resolution of ERA5 Precipitable Water Vapor Using InSAR Data

Pedro Mateus, João Catalão, and Giovanni Nico, *Senior Member, IEEE*

***Abstract*— The interferometric synthetic aperture radar (InSAR) technique has demonstrated its ability to capture temporal variations in tropospheric water vapor, providing a valuable source of information for numerical weather prediction (NWP) models. Integrating InSAR data into NWP models has the potential to significantly enhance their forecasting capabilities, especially for predicting local extreme weather events. The challenge lies in extracting a single epoch from the InSAR differential observations. In this work, we introduced a method based on the least-squares approach to estimate single epochs using the ERA5 reanalysis data from the European Centre for Medium-Range Weather Forecasts (ECMWFs) as a first guess. By leveraging ERA5 data, distinct atmospheric components can be disentangled without additional assumptions or external measurements. Since ERA5 is globally available at 1-h temporal resolution, the proposed method can be applied in remote areas without in situ data, providing improved high-resolution maps at all times (day/night) and in all weather conditions.**

***Index Terms*— Interferometric synthetic aperture radar (InSAR), least-squares method, numerical weather prediction (NWP) model, precipitable water vapor (PWV), reanalysis data.**

I. Introduction

WATER vapor plays a vital role in the planet's energy balance, directly intertwined with the formation of clouds, precipitation, and extreme weather events [1]. Understanding and accurately predicting its distribution and behavior in the atmosphere is essential for advancing our knowledge of weather systems and climate change. One of the key advantages of interferometric synthetic aperture radar (InSAR) is its ability to provide high-resolution spatial maps of water vapor distribution [2], [3]. Traditional weather observation methods, such as weather stations and radiosondes, have limited spatial coverage and may not capture the fine-scale fluctuations of water vapor across a region. Conversely, InSAR can provide precise maps of integrated water vapor with a spatial resolution finer than 100 m. By assimilating InSAR-based water vapor maps into numerical weather prediction (NWP) models, the prediction capability of these models can be significantly enhanced, particularly in the case of local extreme weather events [4], [5], [6]. InSAR measures the phase differences between the acquisition times of SAR images, which are sensitive to changes in the atmosphere. This differential nature presents a challenge when trying to obtain single-epoch maps. Another challenge is the introduction of an unknown bias during the phase unwrapping process, an essential step in InSAR processing [7]. Despite these challenges, researchers have developed methodologies to mitigate the differential nature's limitations in InSAR. These include incorporating additional data sources such as Global Navigation Satellite System (GNSS) measurements, NWP data, or optical missions, for example, imaging spectrometer sensors (MEDIS, MODIS, Sentinel-2, etc.), to represent a time when the atmospheric conditions are known. For example, Pichelli et al. [8] retrieved water vapor maps simultaneously with radar image acquisitions using MERIS observations. However, this was only feasible with the ENVISAT mission, which carried both sensors. Nonetheless, obtaining optical images was not always possible due to cloud cover or lack of sunlight. Mateus et al. [5], [9], [10], [11], [12] and Miranda et al. [13] create a reference map using reanalysis products (ERA-Interim and ERA5) to depict known atmospheric conditions. However, acquiring such reference images can be challenging, especially in atmospheric turbulence conditions. Lagasio et al. [6] applied a similar approach using the generic atmospheric correction online (GACOS) product. Pierdicca et al. [4] proposed an improved reference image combining NWP data and GNSS observations using the 3-D variational assimilation approach. Mulder et al. [14] combine InSAR time series with prior NWP data using a constrained least-squares method (CLQM) to provide an absolute reference to the InSAR estimates. For a systematic comparison of various methods to obtain the absolute reference map, see [15].

We present a new method for estimating the absolute epoch from InSAR data that relies solely on the ERA5 reanalysis data. The suggested method employs a least-squares estimate using the ERA5 precipitable water vapor (PWV) fields as the first guess. The ERA5 data will allow us to separate the various atmospheric components without the need for any further assumptions or measurements. Furthermore, the absolute signal can be calculated at any spatial resolution and promptly digested into NWP models using the proposed method.

Manuscript received 28 February 2024; accepted 15 March 2024. Date of publication 19 March 2024; date of current version 2 April 2024. This work was funded by the Portuguese Fundação para a Ciência e a Tecnologia (FCT) I.P./MCTES through national funds (PIDDAC) – UIDB/50019/2020 (https://doi.org/10.54499/UIDB/50019/2020), UIDP/50019/2020 (https://doi.org/10.54499/UIDP/50019/2020) and LA/P/0068/2020 (https://doi.org/10.54499/LA/P/0068/2020); and in part by Project 2022.15714.MIT. *(Corresponding author: Pedro Mateus.)*

Pedro Mateus and João Catalão are with the Instituto Dom Luiz (IDL), Faculdade de Ciências, Universidade de Lisboa, 1749-016 Lisbon, Portugal (e-mail: pjmateus@ciencias.ulisboa.pt; jcfernandes@ciencias.ulisboa.pt).

Giovanni Nico is with the Istituto per le Applicazioni del Calcolo (IAC), Consiglio Nazionale delle Ricerche (CNR), 70126 Bari, Italy (e-mail: g.nico@ba.iac.cnr.it).

Digital Object Identifier 10.1109/LGRS.2024.3379249

II. Data and Methods

A. Interferometric SAR

A set of 58 single-look complex (SLC) images acquired by the Sentinel-1 mission over the Houston region, the most populous city in the state of Texas, US, were used to generate 165 interferograms. All images were obtained along the relative orbit number 143 in descending flight direction. Twenty-nine images were acquired by Sentinel-1A and the other 29 by Sentinel-1B between January 8 and December 28, 2017, at around 12:20 UTC. The interferograms were generated by merging satellite (A and B) acquisitions. Except for the last two dates, three interferograms were created for each date (reference image), with a 6-, 12-, and 18-day temporal baseline. A maximum temporal baseline of 18 days was chosen to avoid the loss of temporal coherence associated with vegetation changes between the acquisition times. Larger intervals can be considered depending on the scattering properties of the region. We used the SNAP software for the interferometric processing. All interferograms were coregistered based on the Sentinel-1 precise orbits, and a high-resolution digital elevation model (∼30 m) was used to correct the topographic phase contribution. A spatial multilook filter was applied to reduce the phase noise before applying a phase unwrapping algorithm, resulting in a spatial resolution of 300 × 300 m^2. No seismic activity was registered during the period. Thus, it is assumed that the interferometric fringes result from changes in the atmospheric conditions and noise at the time of image acquisition. The phase unwrapping algorithm is a crucial step that must be tuned for an optimized result. In this study, we employed the Bayesian methodology proposed in [16].

B. ERA5 Data

ERA5 is the fifth-generation reanalysis developed by the European Centre for Medium-Range Weather Forecasts (ECMWFs). It provides detailed information about the Earth's atmosphere, including meteorological parameters, on a global scale and at high temporal (1 h) and spatial resolutions (∼30 km). PWV fields (already calculated) are obtained from the final release at https://cds.climate.copernicus.eu/ (single-level dataset). To obtain the PWV fields close to the SLC image acquisition times, two ERA5 PWV fields (at 12:00 and 13:00 UTC) are used to estimate a new ERA5 PWV field at 12:20 UTC (using linear interpolation). This step is necessary to account for the water vapor high variability in space and time. Finally, a bilinear interpolation is applied to the ERA5 PWV maps to obtain the InSAR spatial resolution.

C. GNSS Data

We used a network of 68 permanent GNSS stations belonging to the continuously operating reference stations (CORS) and SuomiNet networks, as well as various Texas public departments. The GAMIT/GLOBK (GG) package is used to estimate 24-h PWV values every 30 min for each GNSS site location with a precision of about 1 mm [17]. A linear interpolation is applied to get the GG PWV simultaneously with SLC image acquisition times (12:20 UTC). The GG PWV data are only used for evaluation purposes. Fig. 1 shows the GNSS network spatial distribution.

D. Estimation of Differential PWV From InSAR

It is assumed that the interferometric fringes are related to changes in the ionosphere and troposphere conditions at the time of acquisition of the SLC images and the system's inherent noise. The ionospheric effects at the C-band are significantly smaller compared to those at the L-band and can be disregarded [18]. The tropospheric phase contribution can be divided into three components: the hydrostatic (dry), related to the dry gases; the non-hydrostatic (wet), related to water vapor molecules; and the liquid component, related to liquid water (water droplets). The dry component is very stable in space. It is mainly canceled due to the differential nature of InSAR, remaining a small signal associated with different atmospheric conditions (temperature and atmospheric pressure) on both image acquisition days. This small dry amount can be accurately calculated (since it does not depend on the turbulent atmospheric part) using NWP data and mitigated from the interferometric phase [19]. In contrast, the liquid component cannot be mitigated without external measurements (e.g., meteorological radar observations). However, their impact is only significant during extreme precipitation occurrences linked with convective systems [20], which were not present during image acquisition days. We can assume that the remaining phase is related to the wet component, and the differential PWV (ΔPWV) can be estimated by

$$\Delta\mathrm{PWV} = \Pi \cdot \frac{\Lambda}{4\pi\rho} \cdot \Delta\Phi \cdot \cos(\vartheta_{\mathrm{look}}) \tag{1}$$

where Λ is the radar wavelength, $\Delta\Phi$ is the unwrapped interferometric phase between two epochs, ρ is the density of water, $\vartheta_{\mathrm{look}}$ is the incidence angle, and Π is a proportionality constant that depends on the weighted mean temperature (T_m) given by

$$\Pi = 10^{-6} R_w \left[k_2' + \frac{k_3}{T_m} \right] \tag{2}$$

where R_w is the specific gas constant water vapor and k_2' and k_3 are refractivity constants [21]. In (2), T_m can be calculated using vertical profiles of water vapor pressure and temperature between the terrain surface and the top of the atmosphere, obtained by radiosondes or NWP models [3].

E. Model and Constrained Least-Squares Setup

The model function to determine the best estimate of the PWV single epoch at dates t_1 (secondary) and t_2 (primary) for a specific geographic location (λ: longitude, φ: latitude) is given by

$$\alpha^{t_1} \mathrm{P}^{t_1}_{\lambda,\varphi} - \alpha^{t_2} \mathrm{P}^{t_2}_{\lambda,\varphi} + \Delta\mathrm{P}^{t_1,t_2}_{\lambda,\varphi} + \delta^{t_1,t_2} = 0 \tag{3}$$

where $\mathrm{P}^{t_1}_{\lambda,\varphi}$ and $\mathrm{P}^{t_2}_{\lambda,\varphi}$ are the PWV for the dates t_1 and t_2 at location (λ, φ), both obtained from the first guess

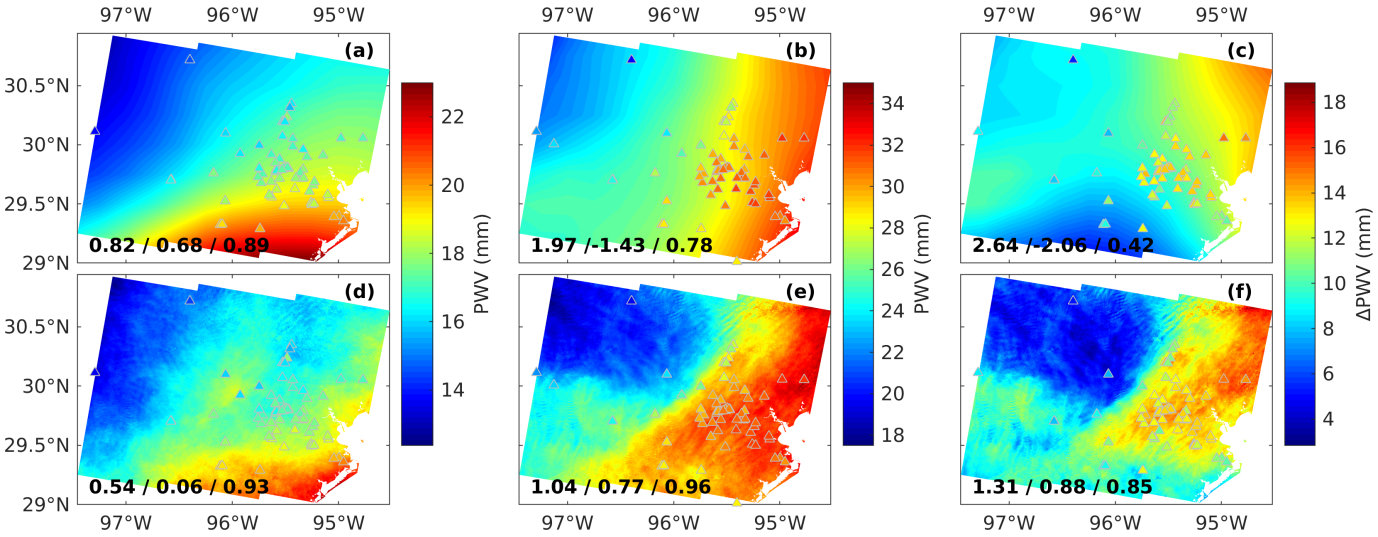

Fig. 1. Application example for doy 32 (first column) and 38 (second column). Upper row: ERA5-A; Lower row: ERA5-B (after CLQM). The triangle shows the GNSS station's locations and color, the corresponding PWV. The bold values at the bottom of the maps are the RMSE, bias, and correlation coefficient (calculated using GNSS PWV as the ground truth). The last column (c) and (f) difference between previous maps, i.e., between (a) and (b) for ERA5-A; and between (d) and (e) for ERA5-B.

(i.e., ERA5, from now on referred to as ERA5-A), $\Delta P^{t_1,t_2}$ is the differential PWV estimated from InSAR (from now on referred to as ERA5-B) using (1), α^{t_1} and α^{t_2} are the constants to estimate by the CLQM, and δ^{t_1,t_2} is a calibrated constant applied to the ΔPWV map due to the arbitrary constant of 2π cycles added by the unwrapped phase algorithm, given by

$$\delta^{t_1,t_2} = \overline{P^{t_2}_{\lambda,\varphi}} - \overline{P^{t_1}_{\lambda,\varphi}} \tag{4}$$

$\overline{P^{t_1}_{\lambda,\varphi}}$ and $\overline{P^{t_2}_{\lambda,\varphi}}$ represent the ERA5 PWV mean at dates t_1 and t_2, respectively. To solve (3), the CLQM is used. This method consists of adjusting the parameters of a model function to best fit a dataset by minimizing the sum of the squares of the residuals, including an additional constraint to the solution [22]. In the sense of the LQM, (3) can be rewritten as

$$A_{n\times m}x_{m\times 1} + \varepsilon_{n\times 1} = Y_{n\times 1} \tag{5}$$

where A is the coefficient matrix, x is the vector of unknown parameters, ε is the vector of residuals, and Y is the analysis state vector. The subscripts refer to the dimension, that is, $n-1$ is the number of interferometric combinations and m is the number of single epochs to estimate. The following equation illustrates the A coefficient configuration of the first three interferometric combinations

$$A_{n\times m} = \begin{bmatrix} \mathrm{P}^{t_1}_{\lambda,\varphi} & -\mathrm{P}^{t_2}_{\lambda,\varphi} & 0 & 0 & \cdots & 0 \\ \mathrm{P}^{t_1}_{\lambda,\varphi} & 0 & -\mathrm{P}^{t_3}_{\lambda,\varphi} & 0 & \cdots & 0 \\ \mathrm{P}^{t_1}_{\lambda,\varphi} & 0 & 0 & -\mathrm{P}^{t_4}_{\lambda,\varphi} & \cdots & 0 \\ \vdots & \vdots & \vdots & \vdots & \ddots & -\mathrm{P}^{t_m}_{\lambda,\varphi} \\ 1 & 1 & 1 & 1 & 1 & 1 \end{bmatrix}. \tag{6}$$

In this case, the first, second, and third line corresponds to the 6-, 12-, and 18-day temporal baseline and the last line corresponds to the additional constraint to the solution, ensuring that the constants to estimate are close to the unit, maintaining the ERA5 mean at each epoch. The below equation illustrates the x, ε, and Y vectors

$$x_{m\times 1} = \begin{bmatrix} \alpha^{t_1}_{\lambda,\varphi} \\ \alpha^{t_2}_{\lambda,\varphi} \\ \alpha^{t_3}_{\lambda,\varphi} \\ \vdots \\ \alpha^{t_m}_{\lambda,\varphi} \end{bmatrix}, \quad \varepsilon_{n\times 1} = \begin{bmatrix} \varepsilon_1 \\ \varepsilon_2 \\ \varepsilon_3 \\ \vdots \\ \varepsilon_n \end{bmatrix}, \text{ and } Y_{n\times 1} = \begin{bmatrix} \Delta\mathrm{P}^{t_1,t_2}_{\lambda,\varphi} + \delta^{t_1,t_2} \\ \Delta\mathrm{P}^{t_1,t_3}_{\lambda,\varphi} + \delta^{t_1,t_3} \\ \Delta\mathrm{P}^{t_1,t_4}_{\lambda,\varphi} + \delta^{t_1,t_4} \\ \vdots \\ \mathrm{m} \end{bmatrix} \tag{7}$$

The following closed-form expression:

$$\hat{x}_{m\times 1} = \left(A^T_{n\times m}C_{n\times n}A_{n\times m}\right)^{-1}A^T_{n\times m}C_{n\times n}Y_{n\times 1} \tag{8}$$

obtained from the CLQM allows for straightforward computation of the estimated parameters ($\hat{x}$). In (8), C is the covariance matrix that measures how the observations are related to each other in terms of their variability. The diagonal elements represent the variances of individual observations, and the off-diagonal elements represent the cross-covariances between pairs of observations. The proposed model is location-based and considering that PWV correlates in time just for minutes to a few hours, depending on the atmospheric conditions, we can assume that all epochs of ERA5 are uncorrelated and have the same accuracy. In this study, C is equal to the identity matrix. The residues (ε) can be calculated after the computation of (8), as

$$\varepsilon_{n\times 1} = Y_{n\times 1} - A_{n\times m}\hat{x}_{m\times 1} \tag{9}$$

Equation (8) is solved for each location (λ, φ), in our case, for each pixel of the ΔPWV map. Considering all

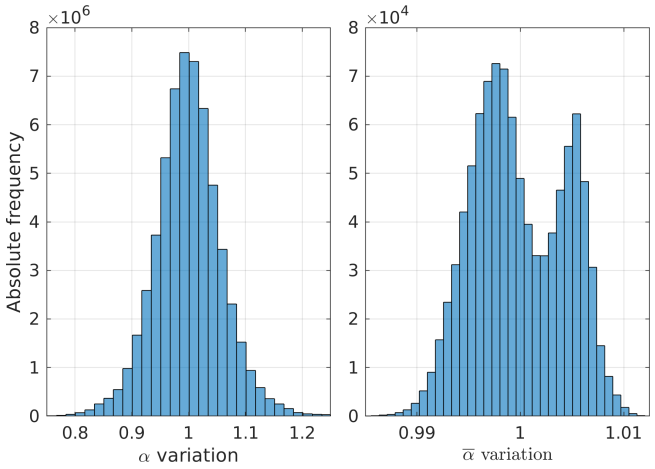

Fig. 2. Left: histogram of the $\alpha^{t_{1-165}}$ (in a pull-together mode); Right: histogram of the $\overline{\alpha^{t_{1-165}}}$.

interferometric combinations (165, ∼1063 700 pixels by interferogram), an overall processing time of about 10 min is needed using an Intel i7 CPU with 12 cores and 32 GB RAM.

III. Results and Discussion

The proposed methodology was applied to the ΔPWV maps generated using 165 interferograms (as described in Section II-A). Fig. 1 shows an example for doy (day-of-year) 32 and 38. The upper line [Fig. 1(a) and (b)] displays the ERA5-A fields, and the lower line [Fig. 1(d) and (e)] the ERA5-B fields (after CLQM). The last column shows the difference between both maps. The triangle color shows the GNSS PWV. ERA5-A and ERA5-B visually display the same longwave signal, and ERA5-B differs by having a more turbulent signal imposed by InSAR maps. The results were assessed using GNSS PWV values and key metrics, including the root-mean-square error (RMSE), bias, and correlation coefficient [23]. The results revealed a substantial improvement in RMSE, demonstrating an enhancement of approximately 50%. Fig. 2 shows two histograms of the α coefficients (values estimated by the CLQM for each single-epoch and geographic location). In the left column for all $\alpha^{t_{1-165}}$, in a pull-together mode, the right column for the $\overline{\alpha^{t_{1-165}}}$ (temporal mean). The parameter α, which ranges from 0.7 to 1.3, is distributed according to a normal distribution with a mean of 0.99 and a standard deviation of 0.01. This behavior is as anticipated, as the constraints imposed by the last equation in the CLQM dictate the range of values that α can take. Analyzing the mean α values (right column), we can distinguish two peaks (bimodal shape). The first, with values lower than 1, are the α values that decrease the ERA5-A values, and the second, with values larger than 1, that increase the ERA5-A values. The larger occurrence of the first peak (related to the second peak) indicates that, on average, ERA5-A exhibits higher water vapor levels than expected. This outcome validates the findings of previous studies [10], [11], [13]. Fig. 3 shows the histograms of the differences between the ΔERA5-B [differences between corresponding ERA5-B epochs, see an example in Fig. 1(f)] and the corresponding ΔPWV maps

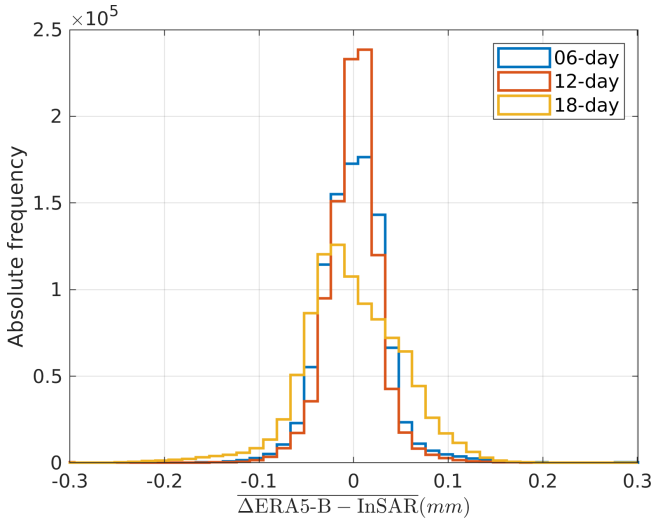

Fig. 3. Histograms of the differences between ΔERA5-B and ΔPWV maps estimated from the interferometric phase. The colors refer to the three combinations (6-, 12-, and 18-day).

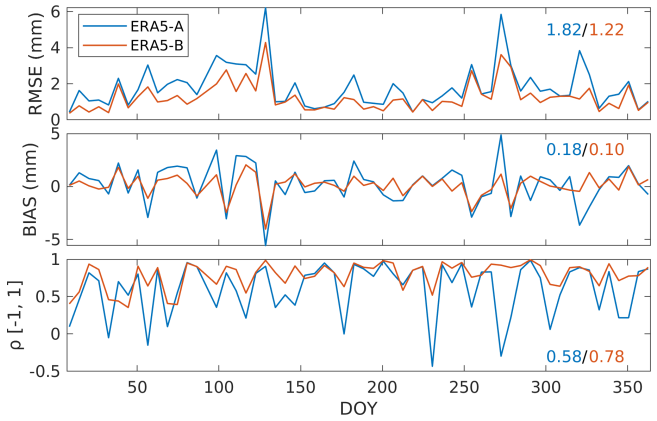

Fig. 4. ERA5-A and ERA5-B evaluation of the 59 single epochs using the GNSS PWV as the "ground truth." The corresponding values on the right indicate the mean value demonstrating the improvement achieved.

[estimated from the interferometric phase and calibrated using (4)]. The 6- and 12-day combinations reveal a mean value close to 0 mm with a standard deviation of 0.04 and 0.03 mm, respectively. However, the 18-day combination shows a slight difference in shape compared to the previous ones, showing a mean value of −0.01 mm and a standard deviation of 0.05 mm. This performance can be related to decreased coherence values obtained for the 18-day interferometric combinations (not shown). Fig. 4 shows a crucial validation of the proposed methodology. We validate the 59 ERA5-A and ERA5-B single epochs with the GNSS PWV observations, considered the "ground truth" here. The impact of the CLQM is always positive or neutral, decreasing the mean RMSE of 1.82 (ERA5-A) to 1.22 mm (ERA5-B) and decreasing the mean bias from 0.18 to 0.10 mm. The correlation coefficient shows the best improvement, from 0.58 to 0.78. The two highest peaks observed in the RMSE series correspond to days when ERA5-A failed to simulate the average water vapor accurately compared to the GNSS observations. However, it correctly captured the spatial pattern on the first day in other aspects. The extent of improvement

in RMSE and bias is limited as the InSAR PWV maps are calibrated based on the ERA5-A spatial mean (over the InSAR footprint). However, the notable enhancements observed in RMSE and bias can be attributed to incorporating small-scale features from InSAR data into ERA5-B. Furthermore, the high correlation coefficient achieved by the CLQM supports the aforementioned statement, reinforcing its validity.

IV. Conclusion

InSAR offers the advantage of providing continuous and all-weather measurements. However, the inherent differential nature of InSAR poses limitations on directly utilizing the phase atmospheric component in NWP models or studying the dynamics of water vapor during extreme events. In this study, we proposed a method based on the least-squares approach to estimate InSAR single epochs using the ERA5 reanalysis data as a first guess. This method uses several InSAR combinations to get redundancy in the system and make use of the ERA5 spatial mean over the InSAR footprint to calibrate the InSAR PWV maps. The results were validated using a considerable GNSS dataset used as ground truth. After applying the proposed technique, the RMSE, bias, and correlation coefficient show a mean improvement of 67%, 55%, and 74%, respectively.

It is worth noting that: 1) the method easily incorporates InSAR small-scale features into the first guess provided by ERA5-A, always showing an improvement, even if limited by the first guess mean; 2) while 18-day InSAR combinations were utilized in this study, alternative combinations can be explored, as their feasibility depends on the characteristics of the scattering surface, indirectly assessed by phase coherence; 3) coherence maps can serve as a means to enforce system weights by leveraging the covariance matrix; and 4) integrating external observations, such as radiosondes or GNSS, is a straightforward process [via (4)], offering the potential to enhance InSAR calibration.

The source of information provided by this method can be used to refine model physical parameterizations, resulting in a more precise representation of water vapor dynamics, especially during convective systems.

References

[1] S. C. Sherwood, R. Roca, T. M. Weckwerth, and N. G. Andronova, "Tropospheric water vapor, convection, and climate," *Rev. Geophysics*, vol. 48, no. 2, Apr. 2010, Art. no. RG2001.

[2] R. F. Hanssen, "Radar interferometry, data interpretation and error analysis," in *Remote Sensing and Digital Image Processing*, vol. 2. Dordrecht, The Netherlands: Springer, 2001, doi: 10.1007/0-306-47633-9.

[3] P. Mateus, G. Nico, and J. Catalão, "Maps of PWV temporal changes by SAR interferometry: A study on the properties of atmosphere's temperature profiles," *IEEE Geosci. Remote Sens. Lett.*, vol. 11, no. 12, pp. 2065–2069, Dec. 2014, doi: 10.1109/LGRS.2014.2318993.

[4] N. Pierdicca et al., "Excess path delays from sentinel interferometry to improve weather forecasts," *IEEE J. Sel. Topics Appl. Earth Observ. Remote Sens.*, vol. 13, pp. 3213–3228, 2020, doi: 10.1109/JSTARS.2020.2988724.

[5] P. Mateus, P. M. A. Miranda, G. Nico, J. Catalão, P. Pinto, and R. Tomé, "Assimilating InSAR maps of water vapor to improve heavy rainfall forecasts: A case study with two successive storms," *J. Geophys. Res., Atmos.*, vol. 123, no. 7, pp. 3341–3355, Apr. 2018, doi: 10.1002/2017jd027472.

[6] M. Lagasio et al., "A synergistic use of a high-resolution numerical weather prediction model and high-resolution Earth observation products to improve precipitation forecast," *Remote Sens.*, vol. 11, no. 20, p. 2387, Oct. 2019, doi: 10.3390/rs11202387.

[7] H. Yu, Y. Lan, Z. Yuan, J. Xu, and H. Lee, "Phase unwrapping in InSAR: A review," *IEEE Geosci. Remote Sens. Mag. Replaces Newsletter*, vol. 7, no. 1, pp. 40–58, Mar. 2019, doi: 10.1109/MGRS.2018.2873644.

[8] E. Pichelli et al., "InSAR water vapor data assimilation into mesoscale model MM5: Technique and pilot study," *IEEE J. Sel. Topics Appl. Earth Observ. Remote Sens.*, vol. 8, no. 8, pp. 3859–3875, Aug. 2015, doi: 10.1109/JSTARS.2014.2357685.

[9] P. Mateus, R. Tomé, G. Nico, and J. Catalão, "Three-dimensional variational assimilation of InSAR PWV using the WRFDA model," *IEEE Trans. Geosci. Remote Sens.*, vol. 54, no. 12, pp. 7323–7330, Dec. 2016, doi: 10.1109/TGRS.2016.2599219.

[10] P. Mateus, P. M. A. Miranda, G. Nico, and J. Catalao, "Continuous multitrack assimilation of Sentinel-1 precipitable water vapor maps for numerical weather prediction: How far can we go with current InSAR data?" *J. Geophys. Res., Atmos.*, vol. 126, no. 3, Feb. 2021, Art. no. e2020JD034171, doi: 10.1029/2020jd034171.

[11] P. Mateus and P. M. A. Miranda, "Using InSAR data to improve the water vapor distribution downstream of the core of the south American low-level jet," *J. Geophys. Res., Atmos.*, vol. 127, no. 7, Apr. 2022, Art. no. e2021JD036111, doi: 10.1029/2021jd036111.

[12] P. Mateus, J. Catalão, G. Nico, and P. Benevides, "Mapping precipitable water vapor time series from Sentinel-1 interferometric SAR," *IEEE Trans. Geosci. Remote Sens.*, vol. 58, no. 2, pp. 1373–1379, Feb. 2020, doi: 10.1109/TGRS.2019.2946077.

[13] P. M. A. Miranda, P. Mateus, G. Nico, J. Catalão, R. Tomé, and M. Nogueira, "InSAR meteorology: High-resolution geodetic data can increase atmospheric predictability," *Geophys. Res. Lett.*, vol. 46, no. 5, pp. 2949–2955, Mar. 2019, doi: 10.1029/2018gl081336.

[14] G. Mulder, F. J. van Leijen, J. Barkmeijer, S. de Haan, and R. F. Hanssen, "Estimating single-epoch integrated atmospheric refractivity from InSAR for assimilation in numerical weather models," *IEEE Trans. Geosci. Remote Sens.*, vol. 60, 2022, Art. no. 4108612, doi: 10.1109/TGRS.2022.3177041.

[15] A. N. Meroni et al., "On the definition of the strategy to obtain absolute InSAR zenith total delay maps for meteorological applications," *Frontiers Earth Sci.*, vol. 8, p. 359, Oct. 2020, doi: 10.3389/feart.2020.00359.

[16] G. Nico and J. Fortuny, "Using the matrix pencil method to solve phase unwrapping," *IEEE Trans. Signal Process.*, vol. 51, no. 3, pp. 886–888, Mar. 2003, doi: 10.1109/TSP.2002.806990.

[17] P. Benevides, J. Catalao, and P. M. A. Miranda, "On the inclusion of GPS precipitable water vapour in the nowcasting of rainfall," *Natural Hazards Earth Syst. Sci.*, vol. 15, no. 12, pp. 2605–2616, Dec. 2015, doi: 10.5194/nhess-15-2605-2015.

[18] C. Liang, P. Agram, M. Simons, and E. J. Fielding, "Ionospheric correction of InSAR time series analysis of C-band Sentinel-1 Tops data," *IEEE Trans. Geosci. Remote Sens.*, vol. 57, no. 9, pp. 6755–6773, Sep. 2019, doi: 10.1109/TGRS.2019.2908494.

[19] P. Mateus, J. Catalão, and G. Nico, "Sentinel-1 interferometric SAR mapping of precipitable water vapor over a country-spanning area," *IEEE Trans. Geosci. Remote Sens.*, vol. 55, no. 5, pp. 2993–2999, May 2017, doi: 10.1109/TGRS.2017.2658342.

[20] Y. Kinoshita, M. Shimada, and M. Furuya, "InSAR observation and numerical modeling of the water vapor signal during a heavy rain: A case study of the 2008 seino event, central Japan," *Geophys. Res. Lett.*, vol. 40, no. 17, pp. 4740–4744, Sep. 2013, doi: 10.1002/grl.50891.

[21] A. M. J. Rüeger, "Refractive index formulae for radio waves," in *Proc. FIG XXII Int. Congr.*, Washington, DC, USA, 2002, pp. 19–26, Accessed: Dec. 19, 2019. [Online]. Available: https://www.gmat.unsw.edu.au

[22] T. Kariya and H. Kurata, *Generalized Least Squares* (Wiley Series in Probability and Statistics), 1st ed. Hoboken, NJ, USA: Wiley, 2004.

[23] D. S. Wilks, *Statistical Methods in the Atmospheric Sciences*, vol. 100, 3rd ed. New York, NY, USA: Academic Press, 2011.